

DeFlowSLAM: Self-Supervised Scene Motion Decomposition for Dynamic Dense SLAM

Weicai Ye*, Xingyuan Yu*, Xinyue Lan, Yuhang Ming, Jinyu Li, Hujun Bao, Zhaopeng Cui and Guofeng Zhang

Abstract—We present a novel dual-flow representation of scene motion that decomposes the optical flow into a static flow field caused by the camera motion and another dynamic flow field caused by the objects’ movements in the scene. Based on this representation, we present a dynamic SLAM, dubbed DeFlowSLAM, that exploits both static and dynamic pixels in the images to solve the camera poses, rather than simply using static background pixels as other dynamic SLAM systems do. We propose a dynamic update module to train our DeFlowSLAM in a self-supervised manner, where a dense bundle adjustment layer takes in estimated static flow fields and the weights controlled by the dynamic mask and outputs the residual of the optimized static flow fields, camera poses, and inverse depths. The static and dynamic flow fields are estimated by warping the current image to the neighboring images, and the optical flow can be obtained by summing the two fields. Extensive experiments demonstrate that DeFlowSLAM generalizes well to both static and dynamic scenes as it exhibits comparable performance to the state-of-the-art DROID-SLAM in static and less dynamic scenes while significantly outperforming DROID-SLAM in highly dynamic environments. Code and data are available on the project webpage: <https://zju3dv.github.io/deflowslam/>.

Index Terms—Dual-Flow Representation, Dynamic Dense SLAM, Dynamic Update Module, Motion Estimation.

I. INTRODUCTION

SIMULTANEOUS localization and mapping (SLAM) is one of the most fundamental tasks in the field of computer vision and robotics, with applications ranging from augmented reality (AR), virtual reality (VR) to autonomous driving. In AR applications, SLAM is often used to provide accurate localization to facilitate users to place virtual objects [1], while the dense reconstruction is increasingly needed for better interaction with the environment. Monocular dense SLAM [2], [3] has received much attention due to the simplicity of monocular video acquisition, yet it is a much more difficult task compared to RGB-D SLAM [4]–[8].

Impressive progress has been seen in geometry-based [9]–[12], learning-based [13]–[15], and hybrid approaches [16]–[18]. However, developing robust and reliable SLAM methods for real-world AR applications is still a challenging problem, especially in dynamic scenarios. To meet the challenges of such dynamic environments, some approaches [19], [20] filter out dynamic objects in advance by introducing information such as semantics, e.g., using Mask R-CNN [21] to segment

W. Ye, X. Yu, X. Lan, J. Li, H. Bao, Z. Cui and G. Zhang are with the State Key Lab of CAD&CG, Zhejiang University. W. Ye, X. Yu, X. Lan, J. Li, H. Bao and G. Zhang are also affiliated with ZJU-SenseTime Joint Lab of 3D Vision. E-mails: {weicaiye, xinyuelan, baohujun, zhpcui, zhang-guofeng}@zju.edu.cn and mail@jinyu.li. Xinyuan Yu is also with Wuhan University. E-mail: RickyYXY@whu.edu.cn. Yuhang Ming is with Visual Information Laboratory, University of Bristol. E-mail: yuhang.ming@bristol.ac.uk.
*: indicates equal contribution. G. Zhang is the corresponding author.

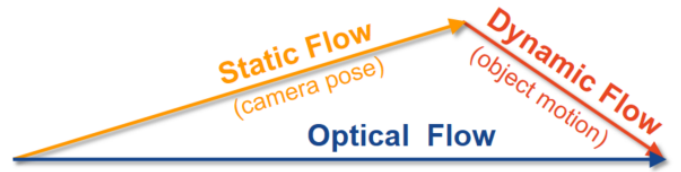


Fig. 1. **Dual-Flow Representation.** The estimated optical flow is decomposed into a static flow caused by the camera poses and a dynamic flow caused by the dynamic object’s motion.

out potentially moving vehicles and pedestrians, and then run monocular SLAM systems such as ORB-SLAM [10]. However, due to the slow running speed and high memory consumption of Mask-RCNN, it is difficult to meet the real-time requirement of SLAM. What’s more, there are limits in practical applications, for not all dynamic objects exist in the detector’s training data and may lead to catastrophic system failure [4]. Besides, simply throwing away dynamic information and only constructing sparse feature maps makes such SLAM methods incapable of handling tasks like planning and interaction. Some approaches [22], [23] combine multi-object detection and SLAM, making it possible to add target-aware constraints to mitigate the interference of dynamic objects, but the generalization of such SLAM systems is limited as well due to the detector.

Recently, a learning-based dense SLAM system, DROID-SLAM [24], has been proposed, which demonstrates better accuracy and robustness than traditional methods. However, we find that it has relatively large errors in the pose estimation in some stronger dynamic scenarios such as sequence 09 of KITTI [25]. DROID-SLAM [24] presents a dense bundle adjustment layer to iteratively update the residual of inverse depths and camera poses using the estimated optical flow and weights, while the presence of dynamic objects may lead to ambiguity in optical flow estimation if the system failed to discover them. For this reason, we propose a novel scene motion representation, named dual-flow, that decomposes the estimated optical flow into a static flow caused by the camera poses and a dynamic flow of the dynamic object’s own motion, as shown in Fig. 1. Such a representation largely mimics the way humans perceive the real world [26]. In addition, DROID-SLAM introduces massive supervision for optical flow, depth, and pose estimation during training, which severely restricts the possibility of finetuning in new scenes if it performs poorly in new scenes. On the contrary, we explore to train our dual-flow-based dynamic SLAM in a self-supervised way.

Our insight is that for the vast majority of scenes, dynamic objects may not be dominant and their motion can be de-

composed by the dominant static objects. The representation based on scene motion decomposition has natural advantages: 1) we can easily optimize static fields in a similar way as DROID-SLAM does for the poses and depths. 2) For dynamic fields, we can obtain consistent luminosity by warping the current frame to adjacent frames. 3) This holds promise for obtaining a self-supervised network model, which is also more interpretable. Based on these observations, we propose a dynamic update module for DeFlowSLAM, in which the dual-flow representation is cleverly embedded, shown in Fig. 2, and detailed in Sec III. Directly warping the dynamic object field to the neighbor images may result in occlusion, shown in Fig. 4, we introduce a dynamic mask aggregation operator in the dynamic update module, named Mask-Agg to remove the incorrect alignment effect. Specifically, the Mask-Agg operator iteratively updates the residuals of the dynamic mask via convolutional gated recurrent unit (ConvGRU). The final dynamic mask can be obtained by summing the aggregated dynamic mask residuals with the original mask. The obtained dynamic mask will be combined with the estimated weights and fed into the dense bundle adjustment (DBA) Layer to optimize the residuals of pose and depth, shown in Fig. 3.

We first verify our hypothesis on a highly dynamic dataset, VKITTI2 [27], where ablation experiments demonstrate that a dual-flow representation can achieve better performance. In addition, DeFlowSLAM can make full use of information from all pixels to solve the camera pose, resulting in gains compared to potential approaches that filter dynamic objects by masking. Applying our knowledge to the challenging SLAM dataset of TartanAir, the trained model exhibits good generalization and achieves comparable accuracy to DROID-SLAM in both static and slightly dynamic scenes. While in highly dynamic scenes, our method significantly outperforms DROID-SLAM, and even the error in pose estimation is sharply reduced to half of DROID-SLAM. Then, we simply extended it to stereo and RGB-D datasets, showing the high scalability of the system. In AR applications, DeFlowSLAM shows relatively accurate pose estimation results, as shown in Fig. 9. In summary, our contributions are three-fold:

- We propose a novel dual-flow scene motion representation that decomposes the optical flow into a static flow field and a dynamic flow field.
- We build a dynamic dense SLAM, DeFlowSLAM, which outperforms state-of-the-art methods in dynamic scenes.
- We propose a self-supervised training method instead of the strong supervision in DROID-SLAM.

II. RELATED WORK

A. Scene Motion Decomposition

Scene motion estimation has received increasing attention for 3D perception. It is the task of obtaining the 3D structure and 3D motion of dynamic scenes. Many scene motion estimation approaches have been proposed recently based on different types of input data, such as 3D point clouds [28], [29], stereo images [30]–[32], or RGB-D images [33]–[36]. Monocular scene flow estimation is a highly ill-posed problem and comparatively few approaches have been suggested so far [37]. Here, we focus on monocular videos and the scene

motion estimation can be regarded as optical flow [38]–[41]. RAFT [42] presents a Recurrent All-pairs Field Transforms network for optical flow estimation, which does not consider the scene motion decomposition. While EffiScene [43] presents an unsupervised scene flow estimation method by jointly learning four low-level vision sub-tasks: optical flow, depth, camera pose, and motion segmentation. Different from the forward and backward flow proposed by DF-VO [44], we leverage the property [45] of the optical flow, where it inherently separates every pixel into multiple moving agents and a large class of points following a single rigid sensor motion and try to decompose the optical flow to the static field caused by the camera pose and dynamic field caused by the objects' own motion.

B. Dynamic SLAM

SLAM is a fundamental capability of many intelligent systems to provide accurate pose estimation and mapping. Humans live in a dynamic environment, intelligent systems should also have the ability to deal with dynamic environments, which are required to recognize the dynamic contents from the static environments. Traditional approaches largely filter out the interference of dynamic objects by introducing a prior [46] or RANSAC methods [47]. Some recent approaches try to use segmentation to filter out potential dynamic objects [19], [20], [48] and then run the SLAM system, or unify object detection and SLAM into a multi-task system [23], [49], [50] or add the object constraint to the SLAM system [22], [51], [52]. Unlike existing approaches, this paper uses a learning-based approach to identify dynamic fields at the pixel level, which does not require explicit supervision of object detection and better simulates the way humans see the world.

C. Dense Reconstruction

Reconstructing dense volumetric scenes is an important task in robotics with many applications such as city modeling, augmented reality navigation [53], and cultural heritage preservation [54]. Most of the existing systems [55]–[59] need to use depth or lidar information for dense reconstruction, this paper does not have this limitation, and can support data formats such as monocular video, stereo, and RGB-D, and can maintain a good reconstruction effect in the dynamic environment. To improve the reconstruction performance, some approaches propose collaborative reconstruction by multiple robots [60]–[62]. As an example, Coxgraph [62] extends the single-robot reconstruction system, Voxgraph [55], to a multi-robot dense reconstruction system, and additionally adds more constraints to ensure low-error reconstruction. Our system is able to maintain robust dense reconstruction with less constraint. Some methods focus on dense depth reconstruction [63]–[65], while our DeFlowSLAM focuses on pose estimation although it can produce the intermediate depth and flow.

III. METHODOLOGY

Fig. 2 shows an overview of our novel dual-flow-based SLAM method, DeFlowSLAM, which takes a sequence of images as input and outputs the estimation of the camera pose and the 3D map of the environments. DeFlowSLAM has an end-to-end differentiable architecture that combines the

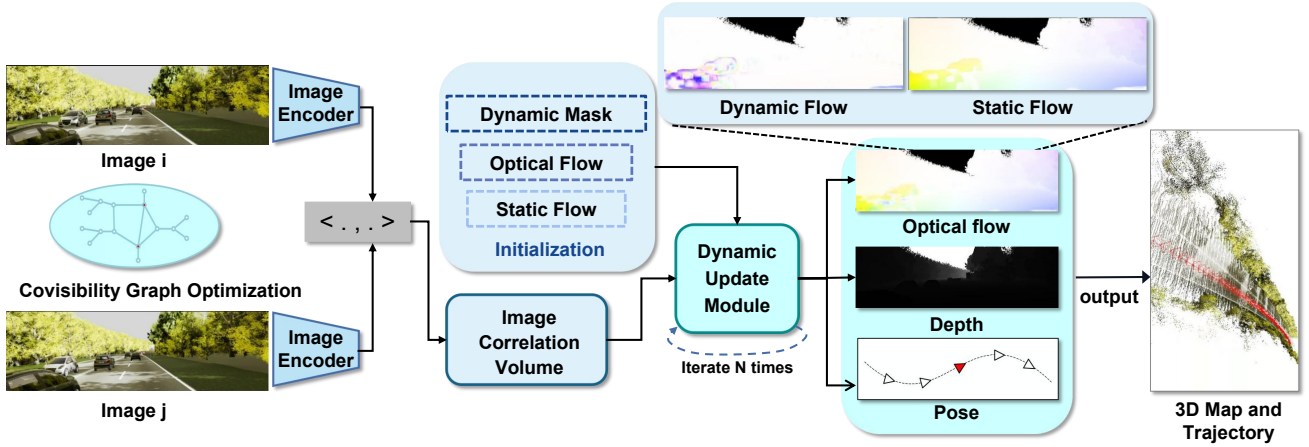


Fig. 2. **DeFlowSLAM Overview.** DeFlowSLAM takes the image sequence as input, extracts features to construct a correlation volume, and feeds it with the initial static flow, optical flow, and dynamic mask into the dynamic update module to iteratively optimize the residual of the pose, inverse depth, static optical flow and dynamic optical flow, and finally outputs the estimation of the camera pose and 3D structure. The optimization process is performed by creating a covisibility graph and updating the existing covisibility graph.

strengths of both classical approaches and deep networks. It can robustly cope with challenging scenarios such as dynamic scenes, thanks to our proposed dual-flow representation, iterative dynamic update module, and factor graph optimization based on co-visibility between frames. Specifically, unlike DROID-SLAM [24], which iteratively updates camera pose and depth, we additionally update a dynamic mask and a dynamic flow. And each update of camera poses in DeFlowSLAM is performed by the optimization of the estimated static flow field rather than the optical flow in DROID-SLAM. Next, we will first review DROID-SLAM for understanding and then elaborate on the details of our approach.

A. Preliminaries: DROID-SLAM

DROID-SLAM [24] operates on a sequence of images $\{\mathbf{I}_t\}_{t=0}^N$. For each image t , it maintains two state variables: camera pose $\mathbf{G}_t \in SE(3)$ and inverse depth $\mathbf{d}_t \in \mathbb{R}_+^{H \times W}$, which get iteratively updated during inference as new frames are processed. DROID-SLAM [24] adopts a frame graph $\mathcal{G} = (\mathcal{V}, \mathcal{E})$ to represent co-visibility between frames. The nodes are input images and the edge $(i, j) \in \mathcal{E}$ implies that the images I_i and I_j have overlapped views.

1) *Feature Extraction and Correlation:* Following RAFT [42], the input images are first fed to the feature extraction module, and the relationship between the two images will be computed.

Feature Extraction. First, each of the input images is processed by an image encoder, which consists of six residual blocks and three downsampling layers. The image encoder produces a dense image feature map, which is 1/8 of the original resolution, and feature maps from pairs of input images are used for later correlation volume construction.

Correlation Pyramid. Given pairs of image features for each edge $(i, j) \in \mathcal{E}$ in the frame graph \mathcal{G} , DROID-SLAM [24] generates the correlation volume by taking the dot product between all-pairs of image feature vectors in $\mathbf{f}_\theta(I_i)_{u_i v_i}$ and $\mathbf{f}_\theta(I_j)_{u_j v_j}$, which has 4 dimensions. It then computes the correlation volume $\mathbf{C}^{ij} \in \mathbb{R}^{H \times W \times H \times W}$ with each element computed as

$$\mathbf{C}_{u_i v_i u_j v_j}^{ij} = \langle \mathbf{f}_\theta(I_i)_{u_i v_i}, \mathbf{f}_\theta(I_j)_{u_j v_j} \rangle. \quad (1)$$

where u_i, v_i, u_j, v_j are the pixel coordinates for image I_i, I_j respectively and $\langle \cdot \rangle$ stands for the dot product. The last two dimensions of the correlation matrix are fed to the average pooling layers with four different kernel sizes (1,2,4,8), forming a 4-level correlation pyramid.

Correlation Lookup. DROID-SLAM [24] defines a correlation lookup function that uses a coordinate grid with radius r to index the correlation volume $L_r : \mathbb{R}^{H \times W \times H \times W} \times \mathbb{R}^{H \times W \times 2} \mapsto \mathbb{R}^{H \times W \times (r+1)^2}$. This function takes an $H \times W$ grid of coordinates as input, which is the dimension of the optical flow field. Then it retrieves the relative values from the correlation volume by using a bi-linear interpolation. The correlation lookup function is applied to every correlation volume matrices in the pyramid. The final output feature is combined by concatenating the lookup results at each level.

2) *Update Module:* DROID-SLAM [24] proposes an update operator, a 3×3 convolutional GRU which updates the hidden state \mathbf{h} , and additionally produces a pose update, $\Delta \xi^{(k)}$, and depth update, $\Delta \mathbf{d}^{(k)}$. In the update module, the pose and depth updates are applied to the current depth and pose estimates through retraction on the SE3 manifold and vector addition respectively

$$\mathbf{G}^{(k+1)} = \text{Exp}(\Delta \xi^{(k)}) \circ \mathbf{G}^{(k)}, \quad \mathbf{d}^{(k+1)} = \Delta \mathbf{d}^{(k)} + \mathbf{d}^{(k)}. \quad (2)$$

The update operator iteratively produces a sequence of poses and depths, with the expectation of converging to a fixed point $\{\mathbf{G}^{(k)}\} \rightarrow \mathbf{G}^*$, $\{\mathbf{d}^{(k)}\} \rightarrow \mathbf{d}^*$, reflecting the true reconstruction.

B. Dual-Flow Representation

The core concept of the proposed dynamic SLAM network is the dual-flow representation and the self-supervised training scheme. In contrast to DROID-SLAM [24], which uses optical flow as an intermediate motion representation, we propose a novel scene motion representation by decomposing optical flow into a static flow caused by camera motion and a dynamic flow caused by the motion of dynamic objects themselves, shown in Fig. 1. Such a representation can distinguish static and dynamic object motions, thus

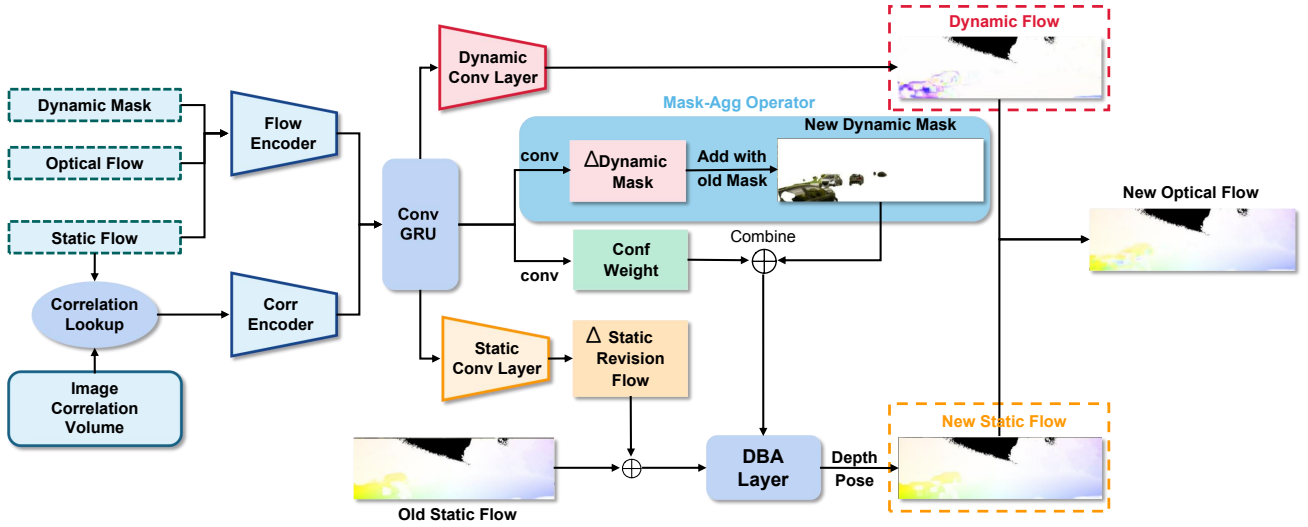


Fig. 3. **Dynamic Update Module.** The correlation feature of the static optical flow is looked up by correlation volumes. The obtained features will be fed into two convolutional layers together with the optical flow and dynamic mask, resulting in intermediate features. These features will be fed to ConvGRU, followed by two convolutional layers with dynamic mask residual and confidence. The iterative dynamic mask residual plus the original mask to obtain the new dynamic mask termed Mask-Agg Operator. In addition, static flow revision and dynamic flow are obtained from the static and dynamic convolution layers. The static revision flow plus the original static flow is fed into the DBA layer that combines the dynamic mask and confidence to optimize the depth and pose. Finally, the new static and dynamic flows from the dynamic convolutional layer are summed to the optical flow.

having better interpretability and making the network traceable during the training process. We can directly use the dense static flow to estimate camera motion without masking out the pixels belonging to dynamic objects. The optical flow $\mathbf{F}_{ot} \in \mathbb{R}^{H \times W \times 2}$, static flow $\mathbf{F}_{st} \in \mathbb{R}^{H \times W \times 2}$ and dynamic flow $\mathbf{F}_{dt} \in \mathbb{R}^{H \times W \times 2}$ are a set of vectors, where the static flow plus the dynamic flow equals the optical flow:

$$\mathbf{F}_{ot} = \mathbf{F}_{st} + \mathbf{F}_{dt}. \quad (3)$$

Our network operates on a sequence of images $\{\mathbf{I}_t\}_{t=0}^N$. As new frames being processed, the set of camera poses $\{\mathbf{G}_t\}_{t=0}^N \in SE(3)$, inverse depths $\{\mathbf{d}_t\}_{t=0}^N \in \mathbb{R}_+^{H \times W}$, static flows $\{\mathbf{F}_{st}\}_{t=0}^N \in \mathbb{R}^{H \times W \times 2}$, dynamic flows $\{\mathbf{F}_{dt}\}_{t=0}^N \in \mathbb{R}^{H \times W \times 2}$ and the binary dynamic masks $\{\mathbf{M}_{dt}\}_{t=0}^N \in \mathbb{R}_+^{H \times W \times 2}$ are updated iteratively. In \mathbf{M}_{dt} , we let 0 indicate dynamic while 1 indicate static. As a reminder in this paper, when we refer to depth, please note that we are using the inverse depth parameterization.

Similar to DROID-SLAM [24], we also adopt a frame graph $\mathcal{G} = (\mathcal{V}, \mathcal{E})$ to represent co-visibility between frames. For example, as shown in the co-visibility graph optimization in Fig. 2, the white nodes indicate each image, and the edges indicate two images with a co-visibility relationship, where the red points indicate image I_i and image I_j , and the blue edges indicate the co-visibility relationship in the frame graph. The frame graphs are built dynamically during the training and inference. After each pose or depth update with the revision static flow field, we can update the frame graph with new co-visibility. When the camera returns to a previously visited place, a long-distance connection is added to the graph, and loop closure is performed.

C. Dynamic Update Module

Fig. 3 shows the dynamic update module of our DeFlowSLAM. The module is a 3×3 ConvGRU with a hidden

state \mathbf{h} . Different from the update module in DROID-SLAM [24], which works directly on the revision optical flow, our dynamic update module works on the decomposed static and dynamic flow fields respectively. We update the revision static flow field in a similar way to DROID-SLAM [24], while for the dynamic flow field, we add it to the static flow field to obtain the optical flow, which is fed into the flow encoder as a new optimization term in the next iteration. Each application of the operator updates the hidden state, and additionally produces a pose increment, depth increment, dynamic mask increment, and dynamic flow. The pose increments are applied to the current pose through retraction on the SE3 manifold,

$$\mathbf{G}^{(k+1)} = \text{Exp}(\Delta \xi^{(k)}) \circ \mathbf{G}^{(k)}. \quad (4)$$

While the depth and the dynamic mask increments are added to the current depth and dynamic mask respectively

$$\Xi^{(k+1)} = \Delta \Xi^{(k)} + \Xi^{(k)}, \quad \Xi \in \{\mathbf{d}, \mathbf{M}_d\}. \quad (5)$$

where $\mathbf{F}_d^{(k+1)}$ is directly given a new value in every iteration. With the updated static flow $\mathbf{F}_s^{(k+1)}$ transformed from $\mathbf{G}^{(k+1)}$ and $\mathbf{d}^{(k+1)}$, the final optical flow can be computed using Equation 3.

Iterative operations of the dynamic update module produce a sequence of poses, depths, dynamic masks, dynamic flows, and complete optical flows with the expectation of converting to an optimal position, such as $\{\mathbf{G}^{(k)}\} \rightarrow \mathbf{G}^*$, $\{\mathbf{d}^{(k)}\} \rightarrow \mathbf{d}^*$, $\{\mathbf{M}_d^{(k)}\} \rightarrow \mathbf{M}_d^*$, $\{\mathbf{F}_d^{(k)}\} \rightarrow \mathbf{F}_d^*$, $\{\mathbf{F}_o^{(k)}\} \rightarrow \mathbf{F}_o^*$, representing the true reconstruction.

1) *Correspondence:* At the beginning of each iteration, we use the current pose and depth estimates to search for correspondence. Given a grid of pixel coordinates, $\mathbf{p}_i \in \mathbb{R}^{H \times W \times 2}$ in frame i , we compute the dense correspondence field \mathbf{p}_{ij}

$$\mathbf{p}_{ij} = \Pi_c(\mathbf{G}_{ij} \circ \Pi_c^{-1}(\mathbf{p}_i, \mathbf{d}_i)), \quad \mathbf{G}_{ij} = \mathbf{G}_j \circ \mathbf{G}_i^{-1}. \quad (6)$$

for each edge $(i, j) \in \mathcal{E}$ in the frame graph. Here Π_c is the camera model that maps a set of 3D points onto the image, and Π_c^{-1} is the inverse projection function that maps the inverse depth map \mathbf{d} and the coordinate grid \mathbf{p}_i to the 3D point cloud. \mathbf{p}_{ij} represents the coordinates of pixel \mathbf{p}_i mapped to j frames using the current pose and depth estimates.

2) *Inputs*: We use the dense correspondence field to index the correlation volumes. For each edge of $(i, j) \in \mathcal{E}$, we use \mathbf{p}_{ij} to lookup from the correlation volume \mathbf{C}^{ij} to retrieve the correlation features. In addition, we use the dense correspondence field to derive the static optical flow caused by the camera motion, i.e., the difference between $\mathbf{p}_{ij} - \mathbf{p}_j$, which is $\mathbf{F}_{s_{ij}}$. For the initial dynamic mask $\mathbf{M}_{d_{ij}}$ and the initial dynamic flow $\mathbf{F}_{d_{ij}}$, we simply initialize them to zeros.

3) *Dynamic Update*: We extract the global context by averaging the hidden states over the spatial dimensions of the image and use this feature vector as an additional input to the ConvGRU. ConvGRU generates an updated hidden state $\mathbf{h}^{(k+1)}$. Instead of directly predicting updates in depth or pose, we predict updates in the space of dense flow fields. We map the hidden states by two additional convolution layers to produce four outputs: (1) a revised static flow field $\mathbf{r}_{s_{ij}} \in \mathbb{R}^{H \times W \times 2}$, (2) an updated dynamic flow field $\mathbf{F}_{d_{ij}} \in \mathbb{R}^{H \times W \times 2}$, (3) a correlation confidence map $\mathbf{w}_{ij} \in \mathbb{R}^{H \times W \times 2}$, (4) an updated dynamic mask increment field $\Delta \mathbf{M}_{d_{ij}} \in \mathbb{R}^{H \times W \times 2}$. The revision \mathbf{r}_{ij} is a correction term for the network prediction, which is used to correct errors in the dense correspondence fields. We express the corrected correspondence as $\mathbf{p}_{s_{ij}}^* = \mathbf{r}_{s_{ij}} + \mathbf{p}_{s_{ij}}$.

We then pool the hidden state's overall features that share the same source view i and predict the pixel-level damping factor λ . We use the softplus operator to ensure that the damping term is positive. In addition, we use pooled features to predict an 8x8 mask that can be used to upsample the inverse depth estimation.

4) *Dense Bundle Adjustment Layer (DBA)*: The dense bundle adjustment layer (DBA) maps a set of stream revisions to a set of pose and pixel depth updates. We define the cost function on the whole frame diagram

$$\mathbf{E}(\mathbf{G}', \mathbf{d}') = \sum_{(i,j) \in \mathcal{E}} \|\mathbf{p}_{s_{ij}}^* - \Pi_c(\mathbf{G}'_{ij} \circ \Pi_c^{-1}(\mathbf{p}_i, \mathbf{d}'_i))\|_{\Sigma_{ij}}^2, \quad (7)$$

$$\Sigma_{ij} = \text{diag } \mathbf{w}_{d_{ij}}, \quad (8)$$

$$\mathbf{w}_{d_{ij}} = \text{sigmoid}(\mathbf{w}_{ij} + (1 - \mathbf{M}_{d_{ij}}) \cdot \eta). \quad (9)$$

where η is set as 10. And $\|\cdot\|_{\Sigma}$ is the Mahalanobis distance, which weights the error term according to the combined confidence $\mathbf{w}_{d_{ij}}$. The combined confidence makes sure that the optimization considers all points. The addition of these points can effectively improve the accuracy of BA operation in dynamic scenes. Equation 7 shows that we want an updated pose \mathbf{G}' and depth \mathbf{d}' such that the reprojected points match the modified correspondence $\mathbf{p}_{s_{ij}}^*$ predicted by the update operator. We use a local parameterization to linearize Equation 7 and use the Gauss-Newton algorithm to solve for the update $(\Delta \xi, \Delta \mathbf{d})$. Since each term in Equation 7 contains only a single depth variable, the Hessian matrix has a block

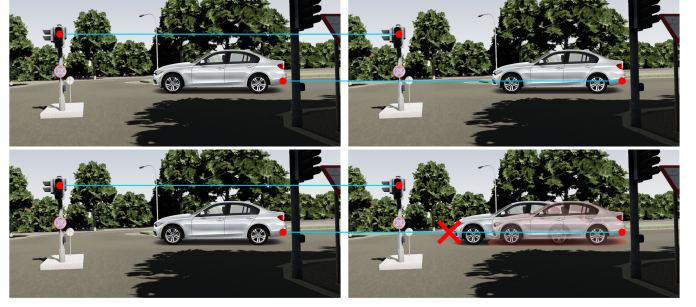


Fig. 4. **Mask-Agg Illustration**. If there are dynamic objects in the scene, directly matching pixels using static flow will cause erroneous results, making photometric loss invalid. Using the aggregated mask predicted by the network, we can filter out these invalid pixels (e.g. the pink mask) in geometry photometric loss, which is shown in the right bottom picture.

diagonal structure. Separating the camera pose and depth variables allows the system to be solved efficiently using Schur's complement and adding the pixel damping factor λ to the depth block. The DBA layer is implemented as part of the computational graph and backpropagation is performed through this layer during training.

D. Loss Function

In this section, we elaborate on the self-supervised training scheme for DeFlowSLAM in detail.

1) *Geometry Photometric Loss*: To supervise the geometry predictions using images, we introduce a photometric reprojection loss to guide the network's optimization. We refer to [66] to build our photometric loss function. Given the predicted pose G_{ij} and the predicted depth $\hat{\mathbf{d}}_i$, we can get the corresponding coordinates of pixels in image I_i in image I_j . We then use bi-linear sampling to sample the image I_j , getting a new-sampled image $I_{j \rightarrow i}$.

$$I_{j \rightarrow i} = I_j \left\langle \Pi_c(\mathbf{G}_{ij} \circ \Pi_c^{-1}(\mathbf{p}_i, \hat{\mathbf{d}}_i)) \right\rangle. \quad (10)$$

Then we can use photometric loss on source image I_i and new image $I_{j \rightarrow i}$.

$$\mathcal{L}_{\text{geo_ph}} = \frac{1}{N} \sum_{ij} pe(I_i, I_{j \rightarrow i}). \quad (11)$$

We introduce L_1 loss and *SSIM* [67] loss to form our geometry photometric loss, setting $\alpha = 0.85$.

$$pe(I_a, I_b) = \frac{\alpha}{2} (1 - \text{SSIM}(I_a, I_b)) + (1 - \alpha) \|I_a - I_b\|_1. \quad (12)$$

2) *Mask Aggregation Operator for Geometry*: In the self-supervised training policy, when using the photometric loss to supervise camera poses and depths, the direct use of the dual-flow representation may result in pixel mismatches due to the object's motion, making the geometry photometric loss less accurate. So we propose a mask aggregation operator, i.e. Mask-Agg, to filter out the wrong pixel matches to enhance our dual-flow representation, as shown in Fig. 4. The aggregated mask $\mathbf{M}_{d_i}^{\text{Agg}}$ for frame I_i is computed by gathering the dynamic masks estimated for all the frames which are connected to frame I_i in the frame graph. Then, the final geometry photometric loss function is

$$\mathcal{L}_{\text{geo_ph}} = \frac{1}{N'} \sum_{ij} pe(I_i, I_{j \rightarrow i}) \cdot \mathbf{M}_{d_i}^{\text{Agg}}. \quad (13)$$

where N' means the count of pixels whose $M_{d_i}^{\text{Agg}}$ value is 1. Specifically, the Mask-Agg operator iteratively updates the residuals of the dynamic mask via ConvGRU. The final dynamic mask can be obtained by summing the aggregated dynamic mask residuals with the original old mask. Tab. I shows the Mask-Agg module helps filter out the ambiguous matches in self-supervised training, obtaining better results.

3) *Optical Flow Photometric Loss*: The geometry photometric loss is used to supervise the static flow caused by camera motion. So we also introduce the optical flow photometric loss to supervise the complete scene motion, including camera motion and objects' motion. Through the update module, we can get the optical flow results $F_{o_{ij}}$ by adding static flow and dynamic flow. Similar to the geometry photometric loss, we use $F_{o_{ij}}$ to generate corresponding coordinates between images.

$$I_{j \rightarrow i} = I_j \langle F_{o_{ij}} + \mathbf{p}_{ij} \rangle. \quad (14)$$

Then we still use bi-linear sampling to sample from the source image, evaluate their photometric errors:

$$\mathcal{L}_{\text{flow_ph}} = \sum_{ij} pe(I_i, I_{j \rightarrow i}). \quad (15)$$

where the pe function here is just L_1 loss:

$$pe(I_a, I_b) = \|I_a - I_b\|_1. \quad (16)$$

4) *Supervised Mask Loss*: When dynamic mask labels are available, we can directly supervise our predicted masks using a simple cross-entropy classification loss:

$$\mathcal{L}_{\text{gt_mask}} = -\frac{1}{|\mathcal{N}|} \sum_{\mathbf{p}_i \in \mathcal{N}} \mathbf{M}_i \log \hat{\mathbf{M}}_i + (1 - \mathbf{M}_i) \log (1 - \hat{\mathbf{M}}_i). \quad (17)$$

where \mathbf{M}_i is the ground truth mask labels, $\hat{\mathbf{M}}_i$ is the predicted masks.

5) *Artificial Mask Loss*: When the dynamic mask labels are not available, we design a method to artificially build referred masks for self-supervised dynamic mask learning. Referred to SLIM [45], we propose the artificial mask loss to achieve this goal. Using the camera pose, depth, and optical flow we have already gotten, we can first infer the target coordinate of the pixel p following the equations below:

$$\mathbf{p}_{\text{cam}} = \Pi_c(\mathbf{G}_{ij} \circ \Pi_c^{-1}(\mathbf{p}_i, \hat{\mathbf{d}}_i)), \mathbf{p}_{\text{flow}} = \mathbf{p}_i + \hat{\mathbf{F}}_{o_{ij}}. \quad (18)$$

where \mathbf{p}_{cam} is the target coordinate calculated by projection, \mathbf{p}_{flow} is the target coordinate calculated by optical flow. Then we use the difference between these two coordinates to form our artificial mask labels

$$\mathbf{M}_i^{\text{art}} = [\|\mathbf{p}_{\text{cam}} - \mathbf{p}_{\text{flow}}\|_2 \leq \mu], \quad (19)$$

where μ is set as 0.5. This artificial mask label has the same format compared with ground truth mask labels, so our final loss function should be

$$\mathcal{L}_{\text{art_mask}} = -\frac{1}{|\mathcal{N}|} \sum_{\mathbf{p}_i \in \mathcal{N}} \mathbf{M}_i^{\text{art}} \log \hat{\mathbf{M}}_i + (1 - \mathbf{M}_i^{\text{art}}) \log (1 - \hat{\mathbf{M}}_i). \quad (20)$$

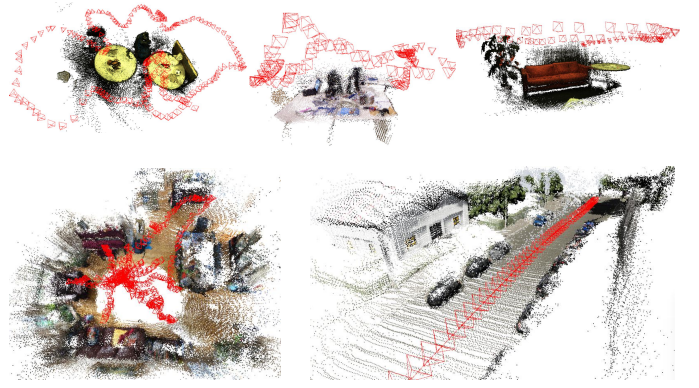


Fig. 5. **Qualitative Results of DeFlowSLAM.** DeFlowSLAM can generalize to new datasets. We show results from ETH3D, TUM RGB-D, ScanNet and Virtual KITTI2.

6) *Final Loss Function*: We use $\mathcal{L}_{\text{geo_ph}}$, $\mathcal{L}_{\text{flow_ph}}$ and $\mathcal{L}_{\text{art_mask}}$ for self-supervised training. The supervised final loss function is

$$\mathcal{L}_{\text{self-sup}} = \lambda_0 \mathcal{L}_{\text{geo_ph}} + \lambda_1 \mathcal{L}_{\text{flow_ph}} + \lambda_2 \mathcal{L}_{\text{art_mask}}. \quad (21)$$

where $\lambda_0 = 100$, $\lambda_1 = 5$, and $\lambda_2 = 0.05$. Since the network has several update iterations, we use $\gamma = 0.9$ to apply the loss to the output of each iteration with exponentially increasing weights. For semi-supervised learning, we modify the $\mathcal{L}_{\text{art_mask}}$ to the $\mathcal{L}_{\text{gt_mask}}$.

E. Implementation Details

1) *Training Details*: DeFlowSLAM is implemented in PyTorch, and we use the LieTorch extension [68] to perform back-propagation in the tangent space of all groups elements. In the ablation study, we trained DeFlowSLAM on the VKITTI2 dataset [27] with 2 RTX-3090 GPUs for 80,000 steps, which took about 2 days. While we trained our network on TartanAir dataset [69] for 250k steps with a batch size of 4 and resolution of 344×464 . Training on 4 RTX-3090 GPUs takes 5 days. In the monocular setup, we fix the first two poses as the true pose for each training sequence as DROID-SLAM [24], for the network can only recover the trajectory of the camera to the similarity transformation. In addition, there are still normative degrees of uncertainty during training, which may have an impact on the stability in terms of regulation and gradients. During training, we set each training example consisting of a 6-frame video sequence. We keep the same constructing strategy in [24], making sure that the average distance between adjacent sequence frames is between 8 pixels and 96 pixels.

2) *SLAM System Details*: In the inference process, we integrate our networks into a full SLAM system. The SLAM system takes the video stream as input and performs simultaneous localization and mapping. Our system contains a frontend thread and a backend thread, both running at the same time. The mission of the frontend thread is to receive new frames, select keyframes, extract features, and perform local bundle adjustment. While the backend thread performs global bundle adjustment for the entire history of keyframes.

Initialization. Following DROID-SLAM [24], our system keeps collecting frames until having 12 frames in total. The

TABLE I

ABLATION STUDY OF DEFLOWSLAM TRAINED AND TESTED ON VIRTUAL KITTII2 (VK) DATASET. SS MEANS SELF-SUPERVISED, SM MEANS SEMI-SUPERVISED, SF MEANS SINGLE FLOW, DF MEANS DUAL FLOW, AND MA MEANS MASK-AGG.

Monocular	VK01	VK02	VK06	VK18	VK20
DROID-SLAM* [24]	1.091	0.025	0.113	1.156	8.285
Ours (SM, DF)	0.761	0.069	0.11	0.737	2.546
Ours (SS, SF)	4.278	0.187	0.142	1.248	10.487
Ours (SS, DF)	1.099	0.094	1.984	0.983	6.918
Ours (SS, DF, MA)	1.341	0.089	0.092	0.376	<u>5.975</u>

TABLE II

ABLATION STUDY OF DYNAMIC THRESHOLD μ OF DEFLOWSLAM TRAINED AND TESTED ON VIRTUAL KITTII2 (VK) DATASET IN SELF-SUPERVISED SETTING. $\mu = 0.5$ ACHIEVES THE BEST RESULTS.

μ	VK01	VK02	VK06	VK18	VK20
0.3	0.763	0.117	0.126	36.10	114.5
0.5	1.341	0.089	0.092	0.376	5.975
0.7	0.738	0.274	0.324	27.41	104.1

system saves the old frame only if its estimated static flow is greater than 16 pixels. Once the system has gotten 12 frames, it initializes the factor graph by creating edges between keyframes within 3 timesteps. Then the system will run the dynamic update operator 10 times using edges in this graph.

Frontend. The frontend directly processes the incoming video stream, which maintains a set of keyframes and a frame graph storing edges between co-visible keyframes, where the keyframe poses and depths are being actively optimized. When a new frame comes, we first extract its feature map, then add it to the frame graph, building edges with its 3 nearest neighbors. The distance used here is measured by averaging static flow. The new frame’s pose is initialized by a linear motion model, and several update iterations are performed to optimize the keyframe poses and depths. We fix the first two poses to eliminate the scale uncertainty while treating all depths as free variables. After tracking the new frame, we use the static flow-based distance to remove redundant frames and remove the oldest keyframe if the buffer is overloaded.

Backend. The backend performs global bundle adjustment over the entire history of keyframes [24]. During each iteration, we first choose the edge whose containing frames are temporally adjacent. We then choose the new edge according to the distance map, which is made by exploiting the averaging static flow between all keyframe pairs. Similar to DROID-SLAM [24], for each chosen edge, we suppress the adjacent edges within a distance of 2, where the distance here is defined as the Chebyshev distance between index pairs $\|(i, j) - (k, l)\|_\infty = \max(|i - k|, |j - l|)$. We then apply the dynamic update operator to the new complete frame graph.

Stereo and RGB-D Inputs. Our system can also use stereo and RGB-D inputs. For RGB-D, we still treat depth as a variable to optimize, since the sensor depth can be noisy. We simply add a term to the optimization process which is shown in Eq. (7). It will then penalize the squared distance between the predicted depths and the sensor depths. For stereo, we use the same system, except for doubling the frames and fixing

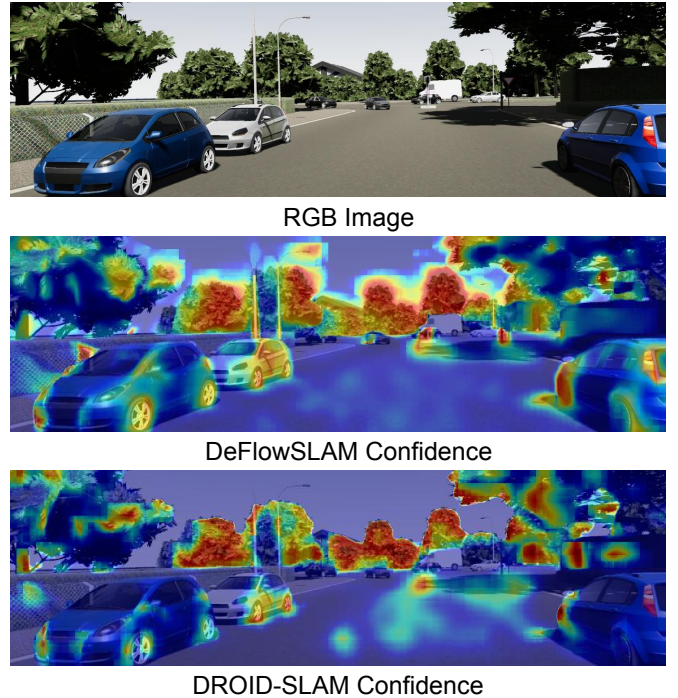


Fig. 6. **DeFlowSLAM Confidence.** We visualize the confidence of our DeFlowSLAM vs. DROID-SLAM. Our method can exploit the dynamic pixels to solve the camera pose. The darker color means the greater weight. DeFlowSLAM also takes advantage of more information about the parked vehicles on the roadside.

TABLE III

DYNAMIC SLAM RESULTS ON KITTI (K) & VIRTUAL KITTII2 (VK) DATASETS WITH METRIC: ATE[M] TRAINED ON TARTANAIR DATASET. WE ACHIEVE THE BEST RESULTS.

Method	K09	K10	VK01	VK02	VK06	VK18	VK20
DSO [12]	<u>28.1</u>	24.0	-	-	-	-	-
DynaSLAM* [19]	41.91	<u>7.519</u>	27.830	X	X	X	<u>2.807</u>
DROID-SLAM* [24]	47.1	11.0	<u>2.259</u>	<u>0.049</u>	<u>0.136</u>	<u>1.170</u>	6.998
Ours	27.8	4.2	0.591	0.021	0.13	0.400	1.039

the relative pose between the left and right frames in the DBA layer. We can exploit the stereo evidence by adding crossed camera edges in the optimization graph [24].

IV. EXPERIMENTS

We first validate the effectiveness of our method in the highly dynamic scenarios of Virtual KITTII2 [27] in the ablation study. Further, we train DeFlowSLAM from scratch with the same strategy on a larger dataset, TartanAir [69], and test the generalization of our method on different dynamic datasets, such as Virtual KITTII2 [27], KITTI [25], and dynamic sequences of TUM-RGBD [70]. We also test monocular or stereo datasets, such as static scenes of TUM-RGBD [70] and EuRoc [71]. Following previous works [24], we use absolute trajectory error (ATE) [72] to evaluate the accuracy of the estimated camera trajectories. In particular, we compare DeFlowSLAM to DynaSLAM [19], etc in dynamic scenes, demonstrating the effectiveness of our method. We also compare DeFlowSLAM to DROID-SLAM in AR applications, the results further prove the robustness of our pose estimation.

A. Datasets

Virtual KITTII2 [27] consists of 5 sequence clones from the KITTI tracking benchmark, and provides different variants of

TABLE IV

DYNAMIC SLAM RESULTS ON TUM DYNAMIC SEQUENCES WITH METRIC: ATE[M]. THE BEST RESULTS ARE SHOWN IN BOLD. DEFLOWSLAM ACHIEVES COMPETITIVE AND EVEN BEST PERFORMANCE. NOTE THAT DVO SLAM, ORB-SLAM2 AND POINTCORR USE THE RGB-D DATASET, WHILE OUR METHOD AND DROID-SLAM ONLY USE THE MONOCULAR RGB DATASET.

Sequences	Trans. RMSE of trajectory alignment [m]					
	DVO SLAM [73]	ORB-SLAM2 [74]	PointCorr [7]	DROID-SLAM [24]	Ours	
slightly dynamic	fr2/desk-person	0.104	0.006	0.008	0.017	0.013
	fr3/sitting-static	0.012	0.008	0.010	0.007	0.007
	fr3/sitting-xyz	0.242	0.010	0.009	0.016	0.015
	fr3/sitting-rpy	0.176	0.025	0.023	0.029	0.027
	fr3/sitting-halosphere	0.220	0.025	0.024	0.022	0.025
highly dynamic	fr3/walking-static	0.752	0.408	0.011	0.016	0.007
	fr3/walking-xyz	1.383	0.722	0.087	0.019	0.018
	fr3/walking-rpy	1.292	0.805	0.161	0.059	0.057
	fr3/walking-halosphere	1.014	0.723	0.035	0.312	0.42

TABLE V

MONOCULAR SLAM RESULTS ON TARTANAIR MONOCULAR BENCHMARK WITH METRIC: ATE[M]. BOLD STANDS FOR BEST RESULTS AND UNDERLINED FOR THE SECOND BEST. * MEANS THE RESULTS ARE GENERATED BY RUNNING THE OFFICIAL PRETRAINED MODEL IN OUR ENVIRONMENT TO ENSURE EVALUATION CONSISTENCY. X MEANS THE SYSTEM HAS FAILED HERE. - MEANS LACK OF RESULT. WE ACHIEVE THE BEST RESULTS.

Monocular	MH000	MH001	MH002	MH003	MH004	MH005	MH006	MH007	Avg
ORB-SLAM [10]	1.30	0.04	2.37	2.45	X	X	21.47	2.73	-
DeepV2D [75]	6.15	2.12	4.54	3.89	<u>2.71</u>	11.55	5.53	3.76	5.03
TartanVO [76]	4.88	0.26	2.00	0.94	1.07	3.19	1.00	2.04	1.92
DROID-SLAM* [24]	0.04	0.69	<u>0.03</u>	<u>0.02</u>	3.73	<u>0.62</u>	<u>0.38</u>	0.07	<u>0.70</u>
Ours	<u>0.63</u>	<u>0.06</u>	0.02	0.01	2.80	0.20	0.31	<u>0.45</u>	0.56

TABLE VI

MONOCULAR SLAM RESULTS ON EUROC DATASET WITH METRIC: ATE[M]. † DENOTES VISUAL ODOMETRY METHODS. X MEANS THE SYSTEM HAS FAILED HERE. - MEANS LACK OF RESULT. WE ACHIEVE COMPARABLE RESULTS ON PAR WITH DROID-SLAM.

		MH01	MH02	MH03	MH04	MH05	V101	V102	V103	V201	V202	V203	Avg
Deep/Hyb.	DeepFactors [2]	1.587	1.479	3.139	5.331	4.002	1.520	0.679	0.900	0.876	1.905	1.021	2.040
	DeepV2D [75]†	0.739	1.144	0.752	1.492	1.567	0.981	0.801	1.570	0.290	2.202	2.743	1.298
	DeepV2D (Tartan Air)†	1.614	1.492	1.635	1.775	1.013	0.717	0.695	1.483	0.839	1.052	0.591	1.173
	TartanVO [76]†	0.639	0.325	0.550	1.153	1.021	0.447	0.389	0.622	0.433	0.749	1.152	0.680
	D3VO + DSO [77]†	-	-	0.08	-	0.09	-	-	0.11	-	0.05	<u>0.19</u>	-
Classical	ORB-SLAM [10]	0.071	0.067	0.071	0.082	0.060	0.015	0.020	X	0.021	<u>0.018</u>	X	-
	DSO [78]†	0.046	0.046	0.172	3.810	0.110	0.089	0.107	0.903	0.044	0.132	1.152	0.601
	SVO [79]†	0.100	0.120	0.410	0.430	0.300	0.070	0.210	X	0.110	0.110	1.080	-
	DSM [80]	0.039	0.036	0.055	<u>0.057</u>	0.067	0.095	0.059	0.076	0.056	0.057	0.784	<u>0.126</u>
	ORB-SLAM3 [81]	<u>0.016</u>	<u>0.027</u>	0.028	0.138	0.072	0.033	0.015	<u>0.033</u>	0.023	0.029	X	-
DROID-SLAM* [24]	0.013	0.014	<u>0.022</u>	0.043	0.043	0.037	<u>0.012</u>	0.020	<u>0.017</u>	0.013	0.014	0.022	
Ours	0.018	0.037	0.020	0.060	<u>0.048</u>	<u>0.031</u>	0.008	0.083	0.016	0.035	1.137	0.136	

these sequences such as modified weather conditions (e.g. fog, rain) or modified camera configurations (e.g. rotated by 15°). In the ablation study, we use the split *clone* as the training set, the split *15-degree rotation* as the validation set, and the split *30-degree rotation* as the test set.

TartanAir [69] is a challenging dataset for robot navigation tasks and SLAM. The data is collected in photo-realistic simulation environments with the presence of moving objects, changing light, and various weather conditions. We use the official test split [69] and calculate ATE in all sequences.

KITTI [25] is a dataset capturing real-world traffic situations and ranges from freeways over rural areas to inner-city scenes with many static and dynamic objects. It contains object labels in the form of 3D tracklets that provides online benchmarks for stereo, optical flow, object detection, and visual odometry.

TUM-RGBD [70] consists of indoor scenes captured with a handheld camera. This is a notoriously difficult dataset for monocular methods due to rolling shutter artifacts, motion blur, and heavy rotation [24]. We use the dynamic sequences to evaluate the effectiveness of DeFlowSLAM in dynamic

scenes and exploit the static sequences in monocular or stereo settings.

EuRoc [71] is a dataset containing 11 sequences classified as simple, medium and difficult based on illumination and camera motion. The dataset [77] is very challenging due to the strong motion and the significant illumination changes between stereo and temporal images. It is a widely used benchmark to evaluate SLAM systems.

B. Ablation Study

We conduct an ablation study to verify the effectiveness of our dual-flow representation in dynamic scenes and further explore the self-supervised training to train our model. We chose Virtual KITTI2 dataset [27] for ablation study.

Framework Design. To remove the interference of dynamic objects, an easy way to implement this is to add a module to DROID-SLAM that removes dynamic objects, which is considered a mask-removal approach. Instead, we use our dual-flow representation to keep more pixels for solving the pose, decomposing the static components even for regions of dynamic objects. Fig. 6 shows that DeFlowSLAM can exploit

TABLE VII

MONOCULAR SLAM RESULTS ON TUM-RGBD DATASET WITH METRIC: ATE[M]. X MEANS THE SYSTEM HAS FAILED HERE. - MEANS LACK OF RESULT. WE ACHIEVE COMPARABLE RESULTS ON PAR WITH DROID-SLAM.

	360	desk	desk2	floor	plant	room	rpy	teddy	xyz	avg
ORB-SLAM2 [74]	X	0.071	X	<u>0.023</u>	X	X	X	X	0.010	-
ORB-SLAM3 [81]	X	<u>0.017</u>	0.210	X	<u>0.034</u>	X	X	X	0.009	-
DeepTAM [82]	0.111	0.053	0.103	0.206	0.064	<u>0.239</u>	0.093	0.144	0.036	0.116
TartanVO [76]	0.178	0.125	0.122	0.349	0.297	0.333	0.049	0.339	0.062	0.206
DeepV2D [75]	0.243	0.166	0.379	1.653	0.203	0.246	0.105	0.316	0.064	0.375
DeepV2D (TartanAir)	0.182	0.652	0.633	0.579	0.582	0.776	0.053	0.602	0.150	0.468
DeepFactors [2]	0.159	0.170	0.253	0.169	0.305	0.364	0.043	0.601	0.035	0.233
DROID-SLAM* [24]	0.111	0.018	<u>0.042</u>	0.021	0.016	0.049	<u>0.026</u>	<u>0.048</u>	0.012	0.038
Ours	0.159	0.016	0.030	0.169	0.048	0.538	0.021	0.039	0.009	<u>0.114</u>

TABLE VIII

STEREO SLAM RESULTS ON TARTANAIR STEREO BENCHMARK WITH METRIC: ATE[M]. X MEANS THE SYSTEM HAS FAILED HERE. - MEANS LACK OF RESULT. WE ACHIEVE COMPARABLE RESULTS ON PAR WITH DROID-SLAM.

Stereo	SH000	SH001	SH002	SH003	SH004	SH005	SH006	SH007	Avg
ORB-SLAM2 [74]	0.05	6.67	X	X	X	X	0.10	X	-
TartanVO [76]	2.52	1.61	3.65	0.29	3.36	4.74	3.72	3.06	2.87
DROID-SLAM* [24]	0.44	0.08	0.13	<u>0.20</u>	<u>0.16</u>	3.29	<u>0.38</u>	<u>0.18</u>	0.61
Ours	<u>0.14</u>	<u>0.10</u>	0.13	0.08	0.09	7.60	0.03	0.02	<u>1.02</u>

TABLE IX

STEREO SLAM RESULTS ON EUROC DATASET WITH METRIC: ATE[M]. - MEANS LACK OF RESULT. WE ACHIEVE COMPARABLE RESULTS ON PAR WITH DROID-SLAM.

	MH01	MH02	MH03	MH04	MH05	V101	V102	V103	V201	V202	V203	Avg
D3VO + DSO [77]	-	-	0.08	-	0.09	-	-	0.11	-	0.05	-	-
ORB-SLAM2 [74]	0.035	0.018	0.028	0.119	0.060	<u>0.035</u>	0.020	<u>0.048</u>	<u>0.037</u>	0.035	-	-
VINS-Fusion [83]	0.540	0.460	0.330	0.780	0.500	0.550	0.230	-	<u>0.230</u>	0.200	-	-
SVO [79]	0.040	0.070	0.270	0.170	0.120	0.040	0.040	0.070	0.050	0.090	0.790	0.159
ORB-SLAM3 [81]	0.029	0.019	<u>0.024</u>	0.085	0.052	<u>0.035</u>	0.025	0.061	0.041	<u>0.028</u>	0.521	0.084
DROID-SLAM* [24]	0.015	<u>0.013</u>	0.035	0.048	0.040	0.037	0.011	0.020	0.018	0.015	0.017	0.024
Ours	<u>0.018</u>	0.011	0.020	<u>0.061</u>	<u>0.042</u>	0.031	0.011	0.090	0.039	0.037	<u>0.478</u>	<u>0.075</u>

the dynamic pixels to solve the camera pose, compared with DROID-SLAM [24]. Tab. I shows that the dual-flow representation is better than the rough single-flow method. Notice that SS means self-supervised, SM means semi-supervised, SF means single flow, and DF means dual flow.

Supervision Policy. We explore the possibility of training DeFlowSLAM in a self-supervised manner. Compared with the supervised approach, which requires a large number of complicated loss functions and is difficult to adjust the appropriate loss weights, and the semi-supervised approach, which requires additional masks for dynamic objects, the self-supervised approach achieves the transformation of different loss functions, allowing a less restricted adaptation to new scenarios and demonstrating better generalization ability. Tab. I demonstrates that the self-supervised approach can achieve comparable or better accuracy than the supervised approach.

Mask-Agg Setting. In self-supervised training, we introduce the Mask-Agg technique to reduce the influence of error matching of the pixels. Because the predicted dynamic masks in self-supervised training are not converged in the early stage of training, we only introduce Mask-Agg at the last 1/10 epochs. Tab. I demonstrates that Mask-Agg helps to improve pose estimation, where MA means Mask-Agg.

Dynamic Threshold μ . In self-supervised setting, we perform an ablation study of dynamic threshold μ on Virtual KITTI2

TABLE X

MOTION SEGMENTATION. WE SHOW THE MOTION SEGMENTATION RESULTS OF DEFLOWSLAM ON VIRTUAL KITTI2 DATASET.

Monocular	VK01	VK02	VK06	VK18	VK20
Ours	0.538585	0.528356	0.562788	0.739282	0.654025

(VK) dataset. Experiments demonstrate that $\mu = 0.5$ achieves the better performance, as shown in Tab. II.

C. Generalization

After verifying the validity of our hypothesis, we trained our DeFlowSLAM on TartanAir dataset [69] from scratch and test our DeFlowSLAM on other popular SLAM datasets, such as Virtual KITTI2 (VKITTI2) [27] and KITTI [25] for autonomous driving scenarios with dynamic objects, EuRoc [71] for drones with strong motion and significant illumination changes, and TUM RGB-D [70] for hand-held SLAM with motion blur and heavy rotations. The results demonstrate that our model generalizes well to different datasets, shown in Figure 5. Next, we show the effectiveness of DeFlowSLAM in several settings.

D. Dynamic SLAM

We test the performance of the proposed DeFlowSLAM on sequences 09 and 10 from KITTI dataset [25] and all

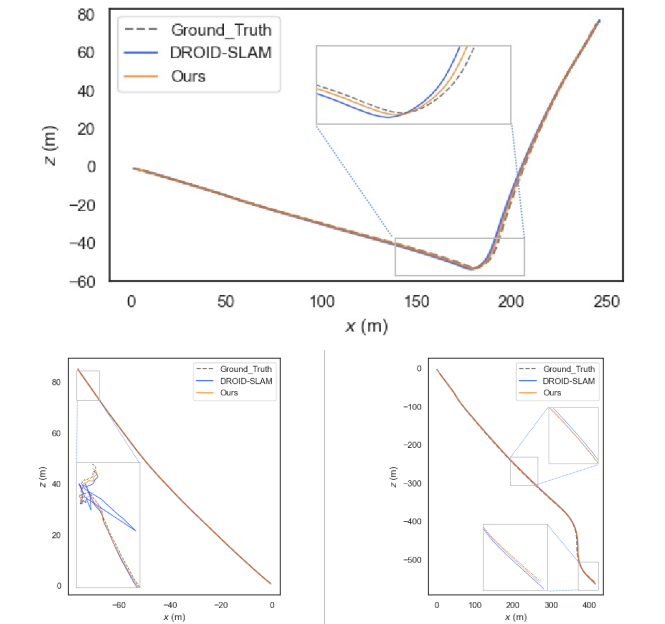


Fig. 7. Comparison Trajectory Results of Our Method with DROID-SLAM on VKITTI2 Sequences 01 (Top), 02 (Bottom-Left), and 20 (Bottom-right). In these dynamic sequences, our method performs better than DROID-SLAM, having better trajectory estimation results.

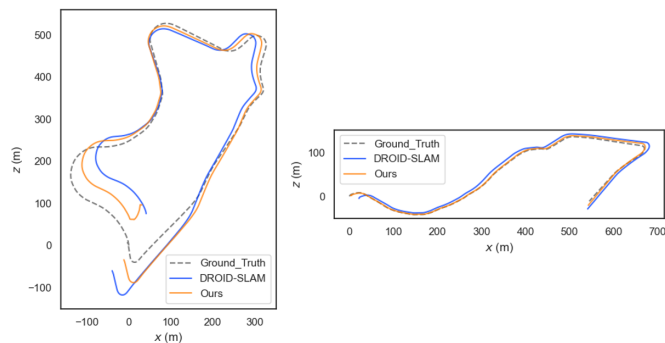


Fig. 8. Trajectory Comparison between Our Method and DROID-SLAM. In KITTI sequences 09 (Left) and 10 (Right), our trajectories are closer to the ground truth.

sequences from Virtual KITTI2 dataset [27]. Here we provide an additional trajectory for this experiment. The ATE results are shown in Table III. Compared with DynaSLAM [19] which uses Mask-RCNN for dynamic environment and DROID-SLAM [24], our DeFlowSLAM is far more accurate and robust in dynamic scenes. We also perform evaluations on TUM RGB-D dynamic sequences with different dynamic proportions and the comparison results in Tab. IV shows that DeFlowSLAM achieves competitive and even best performance. Note that DVO SLAM [73], ORB-SLAM2 [74] and PointCorr [7] use the RGB-D dataset, while our method and DROID-SLAM [24] only use the monocular RGB dataset.

E. Monocular SLAM

In monocular setting, we test our trained DeFlowSLAM on TartanAir test sets, EuRoC, and TUM RGB-D dataset. As shown in Tab. V, DeFlowSLAM achieves the best results. Tab. VI and Tab. VII show that our method achieves comparable even better results than the SOTA supervised method, DROID-SLAM [24] in most sequences. The results

also demonstrate our DeFlowSLAM is more robust than the classical SLAM algorithms as they failed in many sequences. Specifically, we achieve an average ATE of 0.136m on EuRoC dataset in the monocular setting, and an average ATE of 0.114m on TUM-RGBD static sequences, outperforming most supervised methods.

F. Stereo SLAM

Under stereo setup, our trained DeFlowSLAM is also tested on TartanAir test dataset and EuRoC stereo dataset. Tab. VIII illustrates DeFlowSLAM achieves comparable results on par with DROID-SLAM [24], with an average ATE of 1.02m on TartanAir stereo test dataset, outperforming TartanVO [84]. Tab. IX shows that DeFlowSLAM exhibits comparable results on EuRoC dataset in the stereo setting with DROID-SLAM [24], outperforming most supervised methods and traditional SLAM, ORB-SLAM3 [81]. In most sequences, our method is on the same order of magnitude as DROID-SLAM [24], which shows the effectiveness of our method.

G. AR Applications

We conduct extensive experiments on AR applications to demonstrate the robustness of DeFlowSLAM. As shown in Fig. 9, we augment the original video with a virtual tree, a car, and a street lamp. Our DeFlowSLAM can deal with the dynamic objects in the scene very well while DROID-SLAM exhibits significant drifts (the red boxes).

H. Motion Segmentation

Although our method focuses on the SLAM system, our dual-flow representation can be well applied to motion segmentation. We simply set a threshold value (such as $\mu = 0.5$) for motion and visualize the pixel points of the dynamic field larger than this threshold to obtain the result of motion segmentation, as shown in Fig. IV-C and Tab. X.

V. DISCUSSION AND LIMITATIONS

Although our system is versatile to many SLAM settings and is more robust to the challenges of dynamic scenes, it can be further improved in the following directions. DeFlowSLAM performs slightly weaker in some scenarios than DROID-SLAM, probably because we use a certain fixed dynamic threshold. We can explore dynamic threshold estimation methods to the challenges of different scenarios. As with droid-SLAM, we have high memory requirements for longer sequences and larger scenes, and our DeFlowSLAM system needs to run in segments. A lightweight and efficient SLAM system is a potential research direction. For some loop closure sequences, we can add loop closure constraints to reduce the drift. Our system focuses more on solving the camera pose, and the depth and optical flow obtained are only 1/8 of the original image size, which is not ideal for tasks like depth estimation and optical flow estimation. An efficient and versatile SLAM system is worthwhile researching. We can also explore dynamic object reconstruction with dynamic dense SLAM.

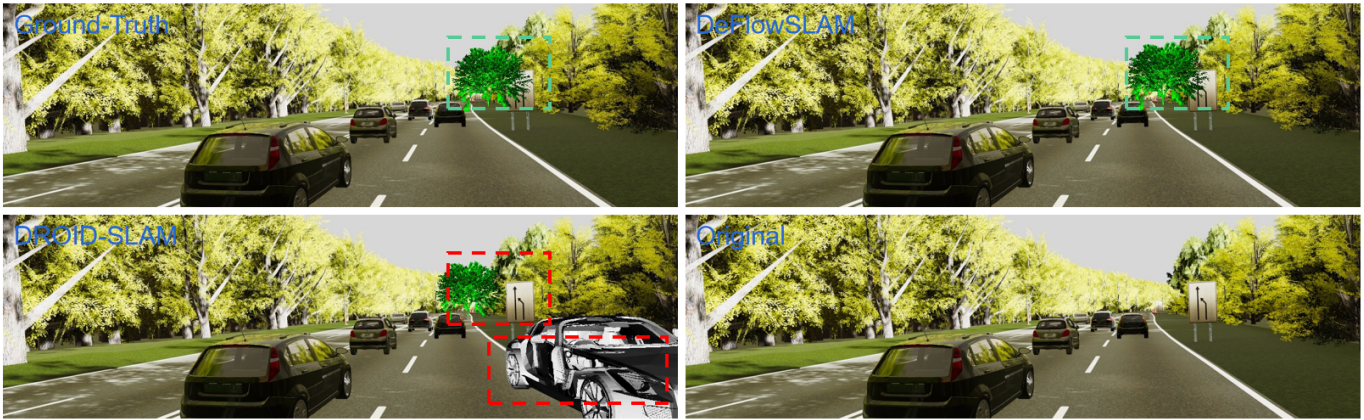


Fig. 9. **AR Application.** DeFlowSLAM deals with the dynamic objects in the scene very well while DROID-SLAM exhibits significant drifts (the red boxes). We augment the original video with a virtual tree, a car, and a street lamp. From left to right and from top to down: Ground-Truth, DeFlowSLAM, DROID-SLAM, Original Image.



Fig. 10. **Motion Segmentation.** From left to right: Ground-Truth dynamic mask, Predicted dynamic mask larger than the dynamic threshold $\mu = 0.5$.

VI. CONCLUSIONS

We present a novel dual-flow representation that decomposes the optical flow into a static flow field caused by the camera poses and a dynamic field caused by the dynamic objects' motion. We present dynamic update module with dual-flow representation to compose the full SLAM system, DeFlowSLAM. We explore a self-supervised method to train our dual-flow based dynamic dense SLAM system, which outperforms DROID-SLAM in highly dynamic scenes and achieves comparable performance in static and slightly dynamic scenes.

ACKNOWLEDGMENTS

This work was partially supported by NSF of China (No. 61932003) and ZJU-SenseTime Joint Lab of 3D Vision.

REFERENCES

- [1] W. Ye, H. Li, T. Zhang, X. Zhou, H. Bao, and G. Zhang, "SuperPlane: 3D Plane Detection and Description from a Single Image," in *IEEE Virtual Reality and 3D User Interfaces*, 2021.
- [2] J. Czarowski, T. Laidlow, R. Clark, and A. J. Davison, "Deepfactors: Real-time probabilistic dense monocular slam," *IEEE Robotics and Automation Letters*, vol. 5, no. 2, pp. 721–728, 2020.
- [3] K. Tateno, F. Tombari, I. Laina, and N. Navab, "Cnn-slam: Real-time dense monocular slam with learned depth prediction," in *Proceedings of the IEEE conference on computer vision and pattern recognition*, 2017, pp. 6243–6252.
- [4] C. Wang, B. Luo, Y. Zhang, Q. Zhao, L. Yin, W. Wang, X. Su, Y. Wang, and C. Li, "Dymslam: 4d dynamic scene reconstruction based on geometrical motion segmentation," *IEEE Robotics and Automation Letters*, 2021.

- [5] L. Yan, X. Hu, L. Zhao, Y. Chen, P. Wei, and H. Xie, "Dgs-slam: A fast and robust rgbd slam in dynamic environments combined by geometric and semantic information," *Remote Sensing*, 2022.
- [6] C. Yu, Z. Liu, X.-J. Liu, F. Xie, Y. Yang, Q. Wei, and Q. Fei, "Ds-slam: A semantic visual slam towards dynamic environments," in *2018 IEEE/RISJ International Conference on Intelligent Robots and Systems (IROS)*. IEEE, 2018, pp. 1168–1174.
- [7] W. Dai, Y. Zhang, P. Li, Z. Fang, and S. Scherer, "Rgb-d slam in dynamic environments using point correlations," *IEEE Transactions on Pattern Analysis and Machine Intelligence*, vol. 44, no. 1, pp. 373–389, 2020.
- [8] M. Henein, J. Zhang, R. Mahony, and V. Ila, "Dynamic slam: the need for speed," in *2020 IEEE International Conference on Robotics and Automation (ICRA)*. IEEE, 2020, pp. 2123–2129.
- [9] J. Engel, T. Schops, and D. Cremers, "LSD-SLAM: Large-scale direct monocular slam," in *ECCV*, 2014.
- [10] R. Mur-Artal, J. M. M. Montiel, and J. D. Tardos, "Orb-slam: a versatile and accurate monocular slam system," *IEEE transactions on robotics*, vol. 31, no. 5, pp. 1147–1163, 2015.
- [11] C. Forster, M. Pizzoli, and D. Scaramuzza, "Svo: Fast semi-direct monocular visual odometry," in *ICRA*. IEEE, 2014, pp. 15–22.
- [12] J. Engel, V. Koltun, and D. Cremers, "Direct sparse odometry," *IEEE transactions on pattern analysis and machine intelligence*, vol. 40, no. 3, pp. 611–625, 2017.
- [13] T. Zhou, M. Brown, N. Snavely, and D. G. Lowe, "Unsupervised learning of depth and ego-motion from video," in *CVPR*, 2017.
- [14] S. Wang, R. Clark, H. Wen, and N. Trigoni, "End-to-end, sequence-to-sequence probabilistic visual odometry through deep neural networks," *The International Journal of Robotics Research*, vol. 37, no. 4-5, pp. 513–542, 2018.
- [15] X. Wang, D. Maturana, S. Yang, W. Wang, Q. Chen, and S. Scherer, "Improving learning-based ego-motion estimation with homomorphism-based losses and drift correction," in *2019 IEEE/RISJ International Conference on Intelligent Robots and Systems (IROS)*. IEEE, 2019, pp. 970–976.
- [16] C. Wang, J. Yuan, and L. Xie, "Non-iterative SLAM," in *International Conference on Advanced Robotics (ICAR)*. IEEE, 2017, pp. 83–90.
- [17] C. Wang, M.-C. Hoang, L. Xie, and J. Yuan, "Non-iterative RGB-D-inertial Odometry," *arXiv preprint arXiv:1710.05502*, 2017.
- [18] S. Brahmbhatt, J. Gu, K. Kim, J. Hays, and J. Kautz, "Geometry-aware learning of maps for camera localization," in *Proceedings of the IEEE Conference on Computer Vision and Pattern Recognition*, 2018.
- [19] B. Bescos, J. M. Facil, J. Civera, and J. Neira, "Dynaslam: Tracking, mapping, and inpainting in dynamic scenes," *IEEE Robotics and Automation Letters*, vol. 3, no. 4, pp. 4076–4083, 2018.
- [20] L. Xiao, J. Wang, X. Qiu, Z. Rong, and X. Zou, "Dynamic-slam: Semantic monocular visual localization and mapping based on deep learning in dynamic environment," *Robotics and Autonomous Systems*, vol. 117, pp. 1–16, 2019.
- [21] K. He, G. Gkioxari, P. Dollar, and R. Girshick, "Mask r-cnn," in *Proceedings of the IEEE International Conference on Computer Vision (ICCV)*, Oct 2017.
- [22] S. Yang and S. Scherer, "Cubeslam: Monocular 3-d object slam," *IEEE Transactions on Robotics*, vol. 35, no. 4, pp. 925–938, 2019.

- [23] J. Huang, S. Yang, T.-J. Mu, and S.-M. Hu, "Clustervo: Clustering moving instances and estimating visual odometry for self and surroundings," in *Proceedings of the IEEE/CVF Conference on Computer Vision and Pattern Recognition*, 2020, pp. 2168–2177.
- [24] Z. Teed and J. Deng, "DROID-SLAM: Deep Visual SLAM for Monocular, Stereo, and RGB-D Cameras," *Advances in neural information processing systems*, 2021.
- [25] A. Geiger, P. Lenz, C. Stiller, and R. Urtasun, "Vision meets robotics: The kitti dataset," *The International Journal of Robotics Research*, vol. 32, no. 11, pp. 1231–1237, 2013.
- [26] J. A. Villacorta-Atienza, C. C. Tapia, S. Díez-Hermano, A. Sánchez-Jiménez, S. Lobov, N. Krilova, A. Murciano, G. E. López-Tolsa, R. Pellón, and V. A. Makarov, "Static internal representation of dynamic situations reveals time compaction in human cognition," *Journal of advanced research*, vol. 28, pp. 111–125, 2021.
- [27] Y. Cabon, N. Murray, and M. Humenberger, "Virtual kitti 2," *arXiv preprint arXiv:2001.10773*, 2020.
- [28] X. Liu, C. R. Qi, and L. J. Guibas, "Flownet3d: Learning scene flow in 3d point clouds," *CVPR*, 2019.
- [29] X. Gu, Y. Wang, C. Wu, Y. J. Lee, and P. Wang, "Hplflownet: Hierarchical permutohedral lattice flownet for scene flow estimation on large-scale point clouds," in *Computer Vision and Pattern Recognition (CVPR), 2019 IEEE International Conference on*, 2019.
- [30] F. Hugué and F. Devernay, "A variational method for scene flow estimation from stereo sequences," in *2007 IEEE 11th International Conference on Computer Vision*. IEEE, 2007, pp. 1–7.
- [31] C. Vogel, K. Schindler, and S. Roth, "Piecewise rigid scene flow," in *Proceedings of the IEEE International Conference on Computer Vision*, 2013, pp. 1377–1384.
- [32] Y. Zhang and C. Kambhampettu, "On 3d scene flow and structure estimation," in *Proceedings of the 2001 IEEE Computer Society Conference on Computer Vision and Pattern Recognition. CVPR 2001*, vol. 2. IEEE, 2001, pp. II–II.
- [33] M. Hornacek, A. Fitzgibbon, and C. Rother, "Sphereflow: 6 dof scene flow from rgb-d pairs," in *Proceedings of the IEEE Conference on Computer Vision and Pattern Recognition*, 2014, pp. 3526–3533.
- [34] S. Hadfield and R. Bowden, "Kinecting the dots: Particle based scene flow from depth sensors," in *2011 International Conference on Computer Vision*. IEEE, 2011, pp. 2290–2295.
- [35] Z. Lv, K. Kim, A. Troccoli, D. Sun, J. Reh, and J. Kautz, "Learning rigidity in dynamic scenes with a moving camera for 3d motion field estimation," in *ECCV*, 2018.
- [36] J. Quiroga, T. Brox, F. Devernay, and J. Crowley, "Dense semi-rigid scene flow estimation from rgbd images," in *European Conference on Computer Vision*. Springer, 2014, pp. 567–582.
- [37] F. Brickwedde, S. Abraham, and R. Mester, "Mono-sf: Multi-view geometry meets single-view depth for monocular scene flow estimation of dynamic traffic scenes," in *Proceedings of the IEEE/CVF International Conference on Computer Vision*, 2019, pp. 2780–2790.
- [38] A. Dosovitskiy, P. Fischer, E. Ilg, P. Hausser, C. Hazirbas, V. Golkov, P. Van Der Smagt, D. Cremers, and T. Brox, "Flownet: Learning optical flow with convolutional networks," in *Proceedings of the IEEE international conference on computer vision*, 2015, pp. 2758–2766.
- [39] E. Ilg, N. Mayer, T. Saikia, M. Keuper, A. Dosovitskiy, and T. Brox, "Flownet 2.0: Evolution of optical flow estimation with deep networks," in *Proceedings of the IEEE conference on computer vision and pattern recognition*, 2017, pp. 2462–2470.
- [40] D. Sun, X. Yang, M.-Y. Liu, and J. Kautz, "Pwc-net: Cnns for optical flow using pyramid, warping, and cost volume," in *Proceedings of the IEEE conference on computer vision and pattern recognition*, 2018, pp. 8934–8943.
- [41] A. Ranjan, V. Jampani, L. Balles, K. Kim, D. Sun, J. Wulff, and M. J. Black, "Competitive collaboration: Joint unsupervised learning of depth, camera motion, optical flow and motion segmentation," in *Proceedings of the IEEE/CVF conference on computer vision and pattern recognition*, 2019, pp. 12 240–12 249.
- [42] Z. Teed and J. Deng, "Raft: Recurrent all-pairs field transforms for optical flow," in *European conference on computer vision*. Springer, 2020, pp. 402–419.
- [43] Y. Jiao, T. D. Tran, and G. Shi, "Effiscene: Efficient per-pixel rigidity inference for unsupervised joint learning of optical flow, depth, camera pose and motion segmentation," in *Proceedings of the IEEE/CVF Conference on Computer Vision and Pattern Recognition (CVPR)*, June 2021, pp. 5538–5547.
- [44] H. Zhan, C. S. Weerasekera, J.-W. Bian, R. Garg, and I. Reid, "Df-vo: What should be learnt for visual odometry?" 2021.
- [45] S. Baur, D. Emmerichs, F. Moosmann, P. Pinggera, B. Ommer, and A. Geiger, "Slim: Self-supervised lidar scene flow and motion segmentation," in *International Conference on Computer Vision (ICCV)*, 2021.
- [46] W. Tan, H. Liu, Z. Dong, G. Zhang, and H. Bao, "Robust monocular slam in dynamic environments," in *2013 IEEE International Symposium on Mixed and Augmented Reality (ISMAR)*. IEEE, 2013, pp. 209–218.
- [47] H. Huang, W.-Y. Lin, S. Liu, D. Zhang, and S.-K. Yeung, "Dual-slam: A framework for robust single camera navigation," in *2020 IEEE/RSJ International Conference on Intelligent Robots and Systems (IROS)*. IEEE, 2020, pp. 4942–4949.
- [48] J. Vincent, M. Labbé, J.-S. Lauzon, F. Grondin, P.-M. Comtois-Rivet, and F. Michaud, "Dynamic object tracking and masking for visual slam," in *2020 IEEE/RSJ International Conference on Intelligent Robots and Systems (IROS)*. IEEE, 2020, pp. 4974–4979.
- [49] G. B. Nair, S. Daga, R. Sajjani, A. Ramesh, J. A. Ansari, K. M. Jatavallabhula, and K. M. Krishna, "Multi-object monocular slam for dynamic environments," in *2020 IEEE Intelligent Vehicles Symposium (IV)*. IEEE, 2020, pp. 651–657.
- [50] W. Ye, X. Lan, S. Chen, Y. Ming, X. Yu, H. Bao, Z. Cui, and G. Zhang, "Pvo: Panoptic visual odometry," 2022.
- [51] M. Strecke and J. Stuckler, "Em-fusion: Dynamic object-level slam with probabilistic data association," in *Proceedings of the IEEE/CVF International Conference on Computer Vision*, 2019, pp. 5865–5874.
- [52] N. Brasch, A. Bozic, J. Lallemand, and F. Tombari, "Semantic monocular slam for highly dynamic environments," in *2018 IEEE/RSJ International Conference on Intelligent Robots and Systems (IROS)*. IEEE, 2018, pp. 393–400.
- [53] O. Wasenmüller, M. Meyer, and D. Stricker, "Augmented reality 3D discrepancy check in industrial applications," *2016 IEEE International Symposium on Mixed and Augmented Reality (ISMAR)*, pp. 125–134, 2016.
- [54] M. Zollhöfer, C. Siegl, M. Vetter, B. Dreyer, M. Stamminger, S. Aybek, and F. Bauer, "Low-cost real-time 3D reconstruction of large-scale excavation sites," *J. Comput. Cult. Herit.*, vol. 9, no. 1, Nov. 2015. [Online]. Available: <https://doi.org/10.1145/2770877>
- [55] V. Reijgwart, A. Millane, H. Oleynikova, R. Siegwart, C. Cadena, and J. Nieto, "Voxgraph: Globally consistent, volumetric mapping using signed distance function submaps," *IEEE Robotics and Automation Letters*, vol. 5, no. 1, pp. 227–234, 2019.
- [56] H. Oleynikova, Z. Taylor, M. Fehr, R. Siegwart, and J. Nieto, "Voxblox: Incremental 3d euclidean signed distance fields for on-board mav planning," in *2017 IEEE/RSJ International Conference on Intelligent Robots and Systems (iros)*. IEEE, 2017, pp. 1366–1373.
- [57] A. Millane, Z. Taylor, H. Oleynikova, J. Nieto, R. Siegwart, and C. Cadena, "C-blox: A scalable and consistent TSDF-based dense mapping approach," in *2018 IEEE/RSJ International Conference on Intelligent Robots and Systems (IROS)*. IEEE, 2018, pp. 995–1002.
- [58] M. Slavcheva, M. Baust, D. Cremers, and S. Ilic, "Killingfusion: Non-rigid 3d reconstruction without correspondences," in *Proceedings of the IEEE Conference on Computer Vision and Pattern Recognition*, 2017, pp. 1386–1395.
- [59] A. Bozic, M. Zollhofer, C. Theobalt, and M. Nießner, "Deepdeform: Learning non-rigid rgb-d reconstruction with semi-supervised data," in *Proceedings of the IEEE/CVF Conference on Computer Vision and Pattern Recognition*, 2020, pp. 7002–7012.
- [60] F. Li, S. Yang, X. Yi, and X. Yang, "CORB-SLAM: a collaborative visual slam system for multiple robots," in *International Conference on Collaborative Computing: Networking, Applications and Worksharing*. Springer, 2017, pp. 480–490.
- [61] P. Schmuck and M. Chli, "CCM-SLAM: Robust and efficient centralized collaborative monocular simultaneous localization and mapping for robotic teams," *Journal of Field Robotics*, vol. 36, no. 4, pp. 763–781, 2019.
- [62] X. Liu, W. Ye, C. Tian, Z. Cui, H. Bao, and G. Zhang, "Coxgraph: Multi-robot collaborative, globally consistent, online dense reconstruction system," in *2021 IEEE/RSJ International Conference on Intelligent Robots and Systems (IROS)*, 2021, pp. 8722–8728.
- [63] F. Wimbauer, N. Yang, L. von Stumberg, N. Zeller, and D. Cremers, "MonoRec: Semi-supervised dense reconstruction in dynamic environments from a single moving camera," in *IEEE Conference on Computer Vision and Pattern Recognition (CVPR)*, 2021.
- [64] R. Ranftl, V. Vineet, Q. Chen, and V. Koltun, "Dense monocular depth estimation in complex dynamic scenes," in *Proceedings of the IEEE conference on computer vision and pattern recognition*, 2016, pp. 4058–4066.

[65] C. Russell, R. Yu, and L. Agapito, "Video pop-up: Monocular 3d reconstruction of dynamic scenes," in *European conference on computer vision*. Springer, 2014, pp. 583–598.

[66] C. Godard, O. M. Aodha, M. Firman, and G. Brostow, "Digging into self-supervised monocular depth estimation," in *2019 IEEE/CVF International Conference on Computer Vision (ICCV)*, 2020.

[67] W. Zhou, A. C. Bovik, H. R. Sheikh, and E. P. Simoncelli, "Image quality assessment: from error visibility to structural similarity," *IEEE Trans Image Process*, 2004.

[68] Z. Teed and J. Deng, "Tangent space backpropagation for 3d transformation groups," in *Conference on Computer Vision and Pattern Recognition*, 2021.

[69] W. Wang, D. Zhu, X. Wang, Y. Hu, Y. Qiu, C. Wang, Y. Hu, A. Kapoor, and S. Scherer, "Tartanair: A dataset to push the limits of visual slam," in *2020 IEEE/RSJ International Conference on Intelligent Robots and Systems (IROS)*, 2020.

[70] D. Schubert, T. Goll, N. Demmel, V. Usenko, J. Stückler, and D. Cremers, "The tum vi benchmark for evaluating visual-inertial odometry," in *IROS*. IEEE, 2018, pp. 1680–1687.

[71] M. Burri, J. Nikolic, P. Gohl, T. Schneider, J. Rehder, S. Omari, M. W. Achtelik, and R. Siegwart, "The euroc micro aerial vehicle datasets," *The International Journal of Robotics Research*, vol. 35, no. 10, pp. 1157–1163, 2016.

[72] J. Sturm, N. Engelhard, F. Endres, W. Burgard, and D. Cremers, "A benchmark for the evaluation of rgb-d slam systems," in *2012 IEEE/RSJ International Conference on Intelligent Robots and Systems*. IEEE, 2012, pp. 573–580.

[73] C. Kerl, J. Sturm, and D. Cremers, "Robust odometry estimation for rgb-d cameras," in *2013 IEEE international conference on robotics and automation*. IEEE, 2013, pp. 3748–3754.

[74] R. Mur-Artal and J. D. Tardós, "Orb-slam2: An open-source slam system for monocular, stereo, and rgb-d cameras," *IEEE Transactions on Robotics*, vol. 33, no. 5, pp. 1255–1262, 2017.

[75] Z. Teed and J. Deng, "Deepv2d: Video to depth with differentiable structure from motion," *arXiv preprint arXiv:1812.04605*, 2018.

[76] W. Wang, Y. Hu, and S. Scherer, "Tartanvo: A generalizable learning-based vo," 2020.

[77] N. Yang, L. v. Stumberg, R. Wang, and D. Cremers, "D3vo: Deep depth, deep pose and deep uncertainty for monocular visual odometry," in *Proceedings of the IEEE/CVF Conference on Computer Vision and Pattern Recognition*, 2020, pp. 1281–1292.

[78] J. Engel, V. Koltun, and D. Cremers, "Direct sparse odometry," *IEEE transactions on pattern analysis and machine intelligence*, vol. 40, no. 3, pp. 611–625, 2017.

[79] C. Forster, Z. Zhang, M. Gassner, M. Werlberger, and D. Scaramuzza, "Svo: Semidirect visual odometry for monocular and multicamera systems," *IEEE Transactions on Robotics*, vol. 33, no. 2, pp. 249–265, 2016.

[80] J. Zubizarreta, I. Aguinaga, and J. M. M. Montiel, "Direct sparse mapping," *IEEE Transactions on Robotics*, vol. 36, no. 4, pp. 1363–1370, 2020.

[81] C. Campos, R. Elvira, J. J. G. Rodríguez, J. M. Montiel, and J. D. Tardós, "Orb-slam3: An accurate open-source library for visual, visual-inertial and multi-map slam," *arXiv preprint arXiv:2007.11898*, 2020.

[82] H. Zhou, B. Ummenhofer, and T. Brox, "Deeptam: Deep tracking and mapping," in *Proceedings of the European conference on computer vision (ECCV)*, 2018, pp. 822–838.

[83] T. Qin and S. Shen, "Online temporal calibration for monocular visual-inertial systems," in *2018 IEEE/RSJ International Conference on Intelligent Robots and Systems (IROS)*. IEEE, 2018, pp. 3662–3669.

[84] W. Wang, Y. Hu, and S. Scherer, "Tartanvo: A generalizable learning-based vo," *arXiv preprint arXiv:2011.00359*, 2020.



Weicai Ye is currently a Ph.D. student in computer science at Zhejiang University, advised by Prof. Hujun Bao and Prof. Guofeng Zhang. He received his B.S. degree in software engineering from University of Electronic Science and Technology of China in 2018. His research interests include SLAM, 3D reconstruction, visual localization, and scene understanding.



Xingyuan Yu is currently a Ph.D. student in computer science at Zhejiang University, advised by Prof. Guofeng Zhang. He received his B.S. degree in computer science and technology from Wuhan University in 2022. His research interests include SLAM and 3D reconstruction.



Xinyue Lan is currently a master's student in software engineering at Zhejiang University, advised by Prof. Guofeng Zhang. She received her B.S. degree in digital media technology from Shandong University in 2020. Her research interests include video panoptic segmentation, and SLAM.



Yuhang Ming is currently a Ph.D. student in computer science at University of Bristol, advised by Prof. Andrew Calway. He received B.E. in Electronic Information Engineering from University of Electronic Science and Technology of China in 2016, B.S. in Electrical Engineering from University of Missouri - Columbia in 2016, and M.S. in Electrical Engineering from University of California, San Diego in 2018. His research interests include SLAM, 3D reconstruction and visual localization.



Jinyu Li is a Ph.D. student of the State Key Lab of CAD&CG, Zhejiang University. Previously, he received his BSc degree in Computer Science and Technology (2011) from Zhejiang University. His research interests include visual-inertial odometry, SLAM, sensor fusion, 3D reconstruction and their applications in virtual/augmented reality and autonomous driving.



reality system SenseMARS.

Hujun Bao is currently a professor in the Computer Science Department of Zhejiang University, and the former director of the state key laboratory of Computer Aided Design and Computer Graphics. His research interests include computer graphics, computer vision and mixed reality. He leads the mixed reality group in the lab to make a wide range of research on 3D reconstruction and modeling, real-time rendering and virtual reality, realtime 3D fusion and augmented reality. Some of these algorithms have been successfully integrated into the mixed



Zhaopeng Cui received the Ph.D. degree from Simon Fraser University in 2017. He was a senior researcher at ETH Zurich. He is currently a research professor in the College of Computer Science, Zhejiang University. His research interests include 3D mapping and localization, 3D scene understanding, image and video editing.



Guofeng Zhang now is a Professor at State Key Lab of CAD&CG, Zhejiang University. He received his BS and Ph.D. degrees in Computer Science from Zhejiang University, in 2003 and 2009, respectively. He received the National Excellent Doctoral Dissertation Award, the Excellent Doctoral Dissertation Award of China Computer Federation and the best paper award of ISMAR 2020. His research interests include structure-from-motion, SLAM, 3D reconstruction, augmented reality, video segmentation, and editing.